ISIJ International, Vol. 37 (1997), No. 8, pp. 748–755

A Mathematical Model for Blast Furnace Reaction Analysis Based on the Four Fluid Model

Peter Richard AUSTIN, Hiroshi NOGAMI and Jun-ichiro YAGI

Institute for Advanced Materials Processing, Tohoku University, Katahira, Aoba-ku, Sendai, Miyagi-ken, 980-77 Japan.

(Received on January 27, 1997; accepted in final form on April 11, 1997)

A two dimensional mathematical model is developed describing four phase chemical reactions, motion, and heat transfer in the blast furnace. The four phases are gas, lump solid, liquid and powder. The model simultaneously calculates the steady state composition, velocity, temperature, and volume fraction of all four phases. The predicted gas, solid and liquid phase compositions are plausible, but the fines dynamic holdup distribution is sensitive to the fines consumption processes in the raceway. The model has also been extended to include silicon transfer reactions. Compared to the base calculations, the predicted cohesive zone position is higher and the bosh is cooler when silicon transfer is included. The model predicts SiO generation from both coke ash silica and molten silica, the latter being the main contributor to hot metal silicon content in the case considered.

KEY WORDS: blast furnace; mathematical model; four fluids; chemical reactions; silicon transfer.

1. Introduction

The blast furnace is a counter current chemical reactor whose main purpose is to reduce iron oxides to iron. The main reductant is carbon, although hydrogen also makes a small contribution. The major materials within the furnace are lump solids (ore and coke), gases and liquids. In modern furnaces using large scale injection of pulverised coal (PC) or other particulate materials, fine solids should also be considered a major phase.

Various mathematical models of the blast furnace have been presented in previous literature.[1–4] However, no reported model considers the four major phases simultaneously interacting *via* multiphase chemical kinetics. In this paper, a model is presented which does consider multiphase chemical reactions, in addition to interphase momentum and heat transfer. This model is an extension of a previously reported model[4] which only solved conservation equations for four phase motion and heat transfer with simplistic representations of the chemical reactions as mass source terms. The present model solves for the composition of all phases, including compositional change due to chemical reactions and the effects of such compositional change on phase properties such as temperature, thermal conductivity and viscosity. The purpose of constructing this model is to demonstrate the feasibility of such an approach, where as many assumptions as possible have been removed from the model, while still retaining computational efficiency and reliability.

An important secondary process occurring in the lower furnace is the transfer of silicon from silica to the hot metal. Silica enters the furnace as a constituent of coke ash and ferrous gangue, and exits as either molten silica in slag or dissolved Si in the hot metal. Numerous studies have shown a variety of transfer routes are possible.[5–9] Silica reduction is an endothermic reaction, which may alter the heat transfer in the lower furnace, thus affecting the hot metal temperature. As an extension to the base model in this report, multiphase silicon transfer is included, and its effect on the thermal state of the bosh investigated.

2. Model Formulation

The two-dimensional, axisymmetric mathematical model considers mass, momentum, enthalpy and chemical species conservation for four phases at steady state. The general conservation equation is given by Eq. (1). Note that the full phase enthalpy is solved for, based on the standard heats of formation and integrated heat capacities of the components of each phase.

$$\frac{\partial}{\partial x}(\varepsilon_i \rho_i u_i \psi) + \frac{1}{r}\frac{\partial}{\partial r}(r \varepsilon_i \rho_i v_i \psi) = \frac{\partial}{\partial x}\left(\varepsilon_i \Gamma_\psi \frac{\partial \psi}{\partial x}\right) + \frac{1}{r}\frac{\partial}{\partial r}\left(r \varepsilon_i \Gamma_\psi \frac{\partial \psi}{\partial r}\right) + S_\psi \quad \text{.....(1)}$$

The four phases considered are gas, lump solids, liquid, and fines. The exchange coefficient, Γ_ψ is non-zero for only two equations. First, for the solid momentum equation, the viscous solids flow model proposed by Chen[10] is used, so Γ_ψ is set to the effective solids viscosity. Second, the solid thermal conductivity is included with modifications to account for radiation and boundary layer conduction.[11,12] The source term S_ψ is

listed in **Table 1** for all ψ.

In the base model, the following chemical species are considered.

- Gas – CO, CO_2, H_2, H_2O, O_2 and N_2.
- Solid – Fe_2O_3 (hematite), Fe_3O_4 (magnetite), Fe_wO (wustite), Fe, gangue in the ferrous burden, C and coke ash. Wustite is a non-stoichiometric compound of variable composition, where w is approximately 0.95.
- Liquid – Fe_wO, Fe, slag and dissolved C.
- Fines – C and ash.

For each phase i, the sum of the chemical species mass fractions is unity.

$$\sum_{j\in i}\omega_{j,i}=1 \quad \text{.....(2)}$$

The conservation equations are solved simultaneously for the four phases using a control volume formulation. All calculations were performed using a grid of 90 axial and 25 radial divisions.

Interphase momentum transfer has been described previously.[4] Interphase heat and mass transfer are discussed in the following sections.

2.1. Interphase Enthalpy Transfer

The gas–solid convective heat transfer coefficient is calculated using a modified form of the Ranz–Marshall[13] equation proposed by Akiyama *et al.*[14]

$$h_{gs}=\frac{k_g}{d_s}(2.0+0.39\,\mathrm{Re}_{gs}^{1/2}\mathrm{Pr}_g^{1/3}) \quad \text{.....(3)}$$

The liquid–solid convective heat transfer coefficient considers resistance in both the solid and liquid phases.[1,15]

$$\frac{1}{h_{sl}}=\frac{1}{h_s}+\frac{1}{h_l} \quad \text{.....(4)}$$

where $$h_l=\frac{k_l}{d_s}\left(\frac{2\sqrt{\mathrm{Re}_{sl}\mathrm{Pr}_l}}{1.55\sqrt{\mathrm{Pr}_l}+3.09\sqrt{0.372-0.15\mathrm{Pr}_l}}\right)$$

and $$h_s=2\sqrt{\frac{k_s C_{P,s}\rho_s|\tilde{u}_l-\tilde{u}_s|}{\pi d_s}}.$$

The fines–solid convective heat transfer coefficient is based on an emulsion model derived for heat transfer between a fluidised bed and a wall.[16] For each of gas–solid, liquid–solid and fines–solid heat transfer, the heat transfer rate is calculated by Eq. (5).

$$\dot{E}_{is}=h_{is}A_{is}(T_i-T_s) \quad \text{for} \quad i=\mathrm{g,\,l,\,f} \quad \text{.....(5)}$$

The liquid–solid contact area is that reported by Niu *et al.*[17]

$$\frac{A_{sl}}{A_s}=0.400\,\mathrm{Re}_{sl}^{0.218}\mathrm{We}_{sl}^{0.0428}\mathrm{Fr}_{sl}^{-0.0238}(1+\cos\theta_{sl})^{-0.0235} \quad \text{.....(6)}$$

where $$A_s=f_{ore}\frac{6\varepsilon_{ore}}{d_{ore}\phi_{ore}}+f_{coke}\frac{6\varepsilon_{coke}}{d_{coke}\phi_{coke}}$$

The gas–solid and fines–solid contact areas are calculated by Eq. (7).

$$A_{is}=\left(\frac{\varepsilon_i}{\varepsilon_g+\varepsilon_f}\right)(A_s-A_{sl}) \quad \text{for} \quad i=\mathrm{g,\,f} \quad \text{.....(7)}$$

Table 1. Source terms in Eq. (1).

ψ	S_ψ
1_g	$M_O\sum_{n=1,6}R_n+M_{CO}R_7+M_C\sum_{n=8,11}R_n+M_C\sum_{n=13,14}R_n$
1_s	$-M_O\sum_{n=1,6}R_n-\sum_{n=15,18}M_jR_n-M_C(R_7+R_8+R_{10}+R_{13}+R_{20})$
1_l	$-M_OR_7+\sum_{n=15,20}M_jR_n$
1_f	$-M_C(R_9+R_{11}+R_{14})-M_{ash}R_{19}$
$\tilde{u}_g$	$-\varepsilon_g\left(\frac{\partial P_g}{\partial x},\frac{\partial P_g}{\partial r}\right)-\tilde{F}_{gs}-\tilde{F}_{gl}-\tilde{F}_{gf}$
$\tilde{u}_s$	$-\varepsilon_s\left(\frac{\partial P_s}{\partial x},\frac{\partial P_s}{\partial r}\right)$
$\tilde{u}_l$	$\varepsilon_l\rho_l\tilde{g}+\tilde{F}_{gl}+\tilde{F}_{sl}$
$\tilde{u}_f$	$\varepsilon_f\rho_f\tilde{g}+\tilde{F}_{gf}+\tilde{F}_{sf}$
H_g†	$-\dot{E}_{gs}-\dot{E}_{gl}-\dot{E}_{gf}+M_O\sum_{n=1,6}\dot{E}_n+M_{CO}\dot{E}_7+M_C\sum_{n=8,11}\dot{E}_n+M_C\sum_{n=13,14}\dot{E}_n$
H_s†	$\dot{E}_{gs}-\dot{E}_{sl}-\dot{E}_{sf}-M_O\sum_{n=1,6}\dot{E}_n-\sum_{n=15,18}M_j\dot{E}_n-M_C(\dot{E}_7+\dot{E}_8+\dot{E}_{10}+\dot{E}_{13}+\dot{E}_{20})$
H_l†	$\dot{E}_{gl}+\dot{E}_{sl}-M_O\dot{E}_7+\sum_{n=15,20}M_j\dot{E}_n$
H_f†	$\dot{E}_{gf}+\dot{E}_{sf}-M_C(\dot{E}_9+\dot{E}_{11}+\dot{E}_{14})-M_{ash}\dot{E}_{19}$

ψ	S_ψ
$\omega_{CO,g}$	$M_{CO}(-R_1-R_2-R_3+R_7+2R_8+2R_9+R_{10}+R_{11}+R_{12}+R_{13}+R_{14})$
$\omega_{CO_2,g}$	$M_{CO_2}(R_1+R_2+R_3-R_8-R_9-R_{12})$
$\omega_{H_2,g}$	$M_{H_2}(-R_4-R_5-R_6+R_{10}+R_{11}-R_{12})$
$\omega_{H_2O,g}$	$M_{H_2O}(R_4+R_5+R_6-R_{10}-R_{11}+R_{12})$
$\omega_{O_2,g}$	$M_{O_2}(-\frac{1}{2}R_{13}-\frac{1}{2}R_{14})$
$\omega_{N_2,g}$	0
$\omega_{Fe_2O_3,s}$	$M_{Fe_2O_3}(-3R_1-3R_4)$
$\omega_{Fe_3O_4,s}$	$M_{Fe_3O_4}(2R_1-\frac{w}{4w-3}R_2+2R_4-\frac{w}{4w-3}R_5)$
$\omega_{Fe_wO,s}$	$M_{Fe_wO}(\frac{3}{4w-3}R_2-R_3+\frac{3}{4w-3}R_5-R_6-R_{16})$
$\omega_{Fe,s}$	$M_{Fe}(wR_3+wR_6-R_{15})$
$\omega_{gangue,s}$	$M_{gangue}(-R_{17})$
$\omega_{C,s}$	$M_C(-R_7-R_8-R_{10}-R_{13}-R_{20})$
$\omega_{ash,s}$	$M_{ash}(-R_{18})$
$\omega_{Fe_wO,l}$	$M_{Fe_wO}(-R_7+R_{16})$
$\omega_{Fe,l}$	$M_{Fe}(wR_7+R_{15})$
$\omega_{slag,l}$	$M_{slag}(R_{17}+R_{18}+R_{19})$
$\omega_{C,l}$	$M_C(R_{20})$
$\omega_{C,f}$	$M_C(-R_9-R_{11}-R_{14})$
$\omega_{ash,f}$	$M_{ash}(-R_{19})$

†Reaction enthalpy source term $\dot{E}_n=R_n\Delta H_n$.

Gas–liquid heat transfer rate is calculated by the method of Mackey and Warner.[18] The gas–fines convective heat transfer coefficient is calculated from the Ranz–Marshall equation.[13] Direct enthalpy transfer from liquid to fines is not considered due to lack of theoretical studies and experimental data.

2.2. Chemical Reactions

Table 2 lists the 15 chemical reactions and 5 phase transformations considered in the model. Note that as the full enthalpy is calculated for each phase, the commonly used heats of reaction are redundant in this model and not included. Rather, the only effect of chemical reactions on enthalpy transport is by interphase enthalpy transfer accompanying mass transfer.

The indirect reduction reactions ($n=1$ to 6) use a three interface shrinking core model.[19] The direct reduction of molten wustite ($n=7$) is actually a three phase reaction, but is simulated as two concurrent reactions involving only two phases each, in order to assign the correct heat transfer sources to the solid, liquid and gas phases. The intermediate species CO (adsorbed on liquid) is generated and consumed at exactly identical rates, thus is not actually solved for. Solution loss ($n=8,9$) and the water gas reaction ($n=10$, 11) gasify carbon from either lump or fine solids. The water gas shift reaction ($n=12$) is homogeneous, so has no accompanying interphase heat transfer source. As this model is not concerned with the details of the raceway, the carbon combustion reactions ($n=13$, 14) are simple linear functions of species concentration. The melting rates ($n=15$ to 19) are assumed proportional to the phase temperature and mass inflow of the species into the control volume. The carbon dissolution rate ($n=20$) is proportional to the difference between the local hot metal carbon content and the aim value specified as the measured carbon content in tapped metal. The scaling factor α_{13} is set based on experience so as to ensure complete consumption of O_2 within the raceway region. The scaling factor α_{14} is iteratively adjusted to enforce a specified PC burnout fraction. The scaling factor α_{20} is set based on experience so that the hot metal carbon content approaches the aim value.

2.3. Physical Properties

2.3.1. Gas

Density is calculated by the ideal gas equation. Viscosity and thermal conductivity are calculated by Wilke's method[25] using component properties calculated from theoretical models.[26,27] Temperature is calculated from Eq. (8), which relates enthalpy to composition and temperature.

$$H_g=\sum_{j\in g}\omega_{j,g}\left[\Delta H_{j,g}^{298\,K}+\int_{298\,K}^{T_g}C_{P,j}(T)dT\right] \quad \text{.....(8)}$$

where $C_{P,j}(T_g)=a_j+b_jT_g+c_jT_g^2$

Heat capacity coefficients are from Ref. 28). Heats of formation are from Ref. 29).

2.3.2. Solid

Ore and coke densities are 3 500 and 1 000 kg/m^3, shape factors are 0.84 and 0.9, viscosities are both 6 Pa·s, and thermal conductivities are both 0.8 W/m·K. The wustite stoichiometric factor w is 0.95. Temperature is calculated

Table 2. Chemical reactions and phase transformations.

n	Formula	Reaction Rate (kmol/m^3·s)	Ref.	Interphase Heat Source (J/kmol)
1	$3Fe_2O_3\,(s)+CO\,(g)\rightarrow 2Fe_3O_4\,(s)+CO_2\,(g)$	† $R_n=\left(\frac{6\varepsilon_{ore}f_{ore}}{\phi_{ore}d_{ore}}\right)\frac{\rho_g}{W}\sum_{m=1,3}\left[a_{n,m}\left(K_m\frac{\omega_{CO,g}}{M_{CO}}-\frac{\omega_{CO_2,g}}{M_{CO_2}}\right)\right]$	20	$\Delta H_n=\Delta H_{CO_2,g}^{T_g}\cdot M_{CO_2}-\Delta H_{CO,g}^{T_g}\cdot M_{CO}$
2	$\frac{w}{4w-3}Fe_3O_4\,(s)+CO\,(g)\rightarrow\frac{3}{4w-3}Fe_wO\,(s)+CO_2\,(g)$			
3	$Fe_wO\,(s)+CO\,(g)\rightarrow wFe\,(s)+CO_2\,(g)$			
4	$3Fe_2O_3\,(s)+H_2\,(g)\rightarrow 2Fe_3O_4\,(s)+H_2O\,(g)$	‡ $R_n=\left(\frac{6\varepsilon_{ore}f_{ore}}{\phi_{ore}d_{ore}}\right)\frac{\rho_g}{W}\sum_{m=4,6}\left[a_{n,m}\left(K_m\frac{\omega_{H_2,g}}{M_{H_2}}-\frac{\omega_{H_2O,g}}{M_{H_2O}}\right)\right]$	20	$\Delta H_n=\Delta H_{H_2O,g}^{T_g}\cdot M_{H_2O}-\Delta H_{H_2,g}^{T_g}\cdot M_{H_2}$
5	$\frac{w}{4w-3}Fe_3O_4\,(s)+H_2\,(g)\rightarrow\frac{3}{4w-3}Fe_wO\,(s)+H_2O\,(g)$			
6	$Fe_wO\,(s)+H_2\,(g)\rightarrow wFe\,(s)+H_2O\,(g)$			
7a	$Fe_wO\,(l)+C\,(s)\rightarrow wFe\,(l)+CO$ (adsorbed on l)	$R_7=k_7\left(\frac{\omega_{Fe_wO,l}\rho_l\varepsilon_l}{M_{Fe_wO}}\right)^2\left(\frac{0.078\times 6\varepsilon_{coke}}{\phi_{coke}d_{coke}}\right)$	21,22	$\Delta H_{7a}=\Delta H_{CO,g}^{T_g}\cdot M_{CO}+w\Delta H_{Fe,l}^{T_g}\cdot M_{Fe}-\Delta H_{Fe_wO,l}^{T_g}\cdot M_{Fe_wO}$
7b	CO (adsorbed on l) $\rightarrow CO\,(g)$			$\Delta H_{7b}=\Delta H_{CO,g}^{T_g}\cdot M_{CO}$
8	$C\,(s)+CO_2\,(g)\rightarrow 2CO\,(g)$ $\quad i=s$	$R_n=\frac{k_{n,1}P_{CO_2}\omega_{C,s}\rho_s\varepsilon_s}{1+k_{n,2}P_{CO}+k_{n,3}P_{CO_2}}$ where $P_j=\frac{\rho_gRT_g}{M_j}\omega_{j,g}$	23	$\Delta H_n=2\Delta H_{CO,g}^{T_l}\cdot M_{CO}-\Delta H_{CO_2,g}^{T_l}\cdot M_{CO_2}$
9	$C\,(f)+CO_2\,(g)\rightarrow 2CO\,(g)$ $\quad i=f$			
10	$C\,(s)+H_2O\,(g)\rightarrow CO\,(g)+H_2\,(g)$ $\quad i=s$	$R_n=\frac{k_{n,4}P_{H_2O}\omega_{C,s}\rho_s\varepsilon_s}{1+k_{n,2}P_{CO}+k_{n,3}P_{CO_2}+k_{n,5}P_{H_2O}}$	24	$\Delta H_n=\Delta H_{CO,g}^{T_l}\cdot M_{CO}+\Delta H_{H_2,g}^{T_l}\cdot M_{H_2}-\Delta H_{H_2O,g}^{T_l}\cdot M_{H_2O}$
11	$C\,(f)+H_2O\,(g)\rightarrow CO\,(g)+H_2\,(g)$ $\quad i=f$			
12	$CO_2\,(g)+H_2\,(g)\leftrightarrow CO\,(g)+H_2O\,(g)$	$R_{12}=f_{ore}\varepsilon_s\left(k_{12,1}+K_{12}k_{12,2}\right)\left(P_{CO}P_{H_2O}-P_{CO_2}P_{H_2}/K_{12}\right)$	20	$\Delta H_{12}=0$
13	$C\,(s)+\frac{1}{2}O_2\,(g)\rightarrow CO\,(g)$	$R_{13}=\alpha_{13}\omega_{O_2,g}$ where α_{13}=0.01	-	$\Delta H_{13}=\Delta H_{C,s}^{T_g}\cdot M_C$
14	$C\,(f)+\frac{1}{2}O_2\,(g)\rightarrow CO\,(g)$	$R_{14}=\alpha_{14}\omega_{O_2,g}\omega_{C,f}$ where α_{14}=100	-	$\Delta H_{14}=\Delta H_{C,f}^{T_l}\cdot M_C$
15	$Fe\,(s)\rightarrow Fe\,(l)$ $\quad i=s\ j=Fe$	$R_n=\left\langle\frac{T_i-T_{min,j}}{T_{max,j}-T_{min,j}}\right\rangle_0^1\cdot\frac{\sum_{inflow}\left(\omega_{j,i}u_i\rho_i\varepsilon_iA_{face}\right)}{M_j\cdot Vol_{cell}}$ where $\langle\psi\rangle_a^b=\max(a,\min(b,\psi))$	-	$\Delta H_n=\Delta H_{j,l}^{T_l}\cdot M_j$ $\quad T_{min}$=1100°C T_{max}=1200°C
16	$Fe_wO\,(s)\rightarrow Fe_wO\,(l)$ $\quad i=s\ j=Fe_wO$			T_{min}=1100°C T_{max}=1200°C
17	Gangue $(s)\rightarrow$ Slag (l) $\quad i=s\ j=gangue$			T_{min}=1100°C T_{max}=1200°C
18	Ash $(s)\rightarrow$ Slag (l) $\quad i=s\ j=ash$			T_{min}=1100°C T_{max}=1200°C
19	Ash $(f)\rightarrow$ Slag (l) $\quad i=f\ j=ash$			T_{min}=1800°C T_{max}=2000°C
20	$C\,(s)\rightarrow[C]\,(l)$	$R_{20}=\frac{\alpha_{20}\varepsilon_l}{M_C}\left(\left[\frac{\omega_{C,l}}{\omega_{C,l}+\omega_{Fe,l}}\right]_{aim}-\frac{\omega_{C,l}}{\omega_{C,l}+\omega_{Fe,l}}\right)$ $\quad \alpha_{20}$=5	-	$\Delta H_{20}=\Delta H_{C,l}^{T_l}\cdot M_C$

†) $a_{1,1}=A_3\left(A_2+B_2+B_3^*\right)+\left(A_2+B_2\right)B_3^*$ $\quad a_{1,2}=a_{2,1}=-\left[A_3\left(B_2+B_3^*\right)+B_2B_3^*\right]$ $\quad A_n=\frac{1}{X_n^2}\cdot\frac{1}{k_n\left(1+1/K_n\right)}$ $\quad B_n=\frac{X_{n+1}-X_n}{X_{n+1}X_n}\cdot\frac{d_s}{2D_n}$ $\quad X_1=\frac{d_{Fe_2O_3}}{d_s}$ $\quad X_3=\frac{d_{Fe_wO}}{d_s}$

$a_{2,2}=\left(A_1+B_1+B_2\right)\left(A_3+B_3^*\right)+A_3B_3^*$ $\quad a_{2,3}=a_{3,2}=-\left(A_1+B_1\right)B_3^*$ $\quad W=\left(A_1+B_1\right)a_{1,1}-A_2a_{1,2}$ $\quad B_3^*=B_3+\frac{1}{k_{film,CO_2}}$ $\quad X_2=\frac{d_{Fe_3O_4}}{d_s}$ $\quad X_4=1$

‡) Coefficients $a_{n,m}$ are calculated as for reactions 1 to 3, replacing 1, 2 and 3 by 4, 5 and 6 respectively.

from Eq. (9).

$$H_s = \sum_{j \in s} \omega_{j,s} \left[\Delta H_{j,s}^{298\,K} + \int_{298\,K}^{T_s} C_{P,j}(T) dT \right] \quad \text{.....(9)}$$

where $C_{P,j}(T_s) = a_j + b_j T_s + c_j / T_s^2$

Heat capacity coefficients and heats of formation are from Ref. 29). Coke carbon was assumed to consist of graphite and amorphous carbon, with an effective heat of formation of $-1\,000$ kJ/kg based on typical coal heating values.[29] Bulk solid properties (ε_s, ϕ_s, μ_s, ρ_s and d_s) are averaged from the ore and coke properties using the local ore/coke volume ratio. The ore/coke volume ratio and particle diameter distributions have been described previously.[4] The viscosity is increased 100-fold in the deadman to restrict flow to the minimum speed necessary to satisfy continuity. This is different to the viscous flow model proposed by Chen,[10] who excluded solid flow from the deadman region. This modification is necessary in order to allow for possible coke consumption within the deadman by various chemical reactions.

2.3.3. Liquid

Liquid droplet diameter is proportional to local solids particle diameter.[30] Shape factor is unity. Slag and metal density, viscosity and thermal conductivity are functions of composition and temperature,[30,31] as listed in **Table 3**. The liquid density, viscosity and thermal conductivity are mass averaged from the metal and slag properties. Heat capacity and temperature are calculated in the same way as for solids. Slag composition is assumed constant, and M_{gangue} and M_{ash} in the solid phase, M_{slag} in the liquid phase, and M_{ash} in the fines phase are all assumed equal to the mean slag molecular weight.

2.3.4. Fines

Particle diameter is 0.1 mm, shape factor is unity, density is 100 kg/m^3 and effective thermal conductivity is 0.1 W/m·K. Heat capacity and temperature are calculated in the same way as for solids.

2.4. Boundary Conditions

The velocity boundary conditions have been described previously.[4] At any point along the wall, the wall heat loss flux is

$$q_{wall} = h_{wall}(T_{ave} - T_{wall}) \quad \text{.....(10)}$$

where $T_{ave} = \alpha_{wall} T_s + (1 - \alpha_{wall}) T_g$

Table 3. Liquid metal and slag properties.

Property	Metal	Slag
ρ_l (kg/m^3)	$8586 - 0.8567T_l - 63 \times [\%C]$	2620
μ_l (Pa·s)	$0.0967 \times 10^{-3} \exp\left(\frac{58.9 \times 10^3}{8.314 T_l}\right)$	$0.1 \times 10^{p\dagger}$
k_l (W/m·K)	$0.0158 T_l$	0.57

† $p = 1.7089\left(\frac{\omega_{CaO,slag}}{\omega_{SiO_2,slag}}\right)^2 - 4.7419\left(\frac{\omega_{CaO,slag}}{\omega_{SiO_2,slag}}\right) + 0.9331\omega_{MgO,slag}^2$
$- 1.8862\omega_{MgO,slag} + 7.9909\omega_{Al_2O_3,slag}^2 - 1.0317\omega_{Al_2O_3,slag}$,
$+ \frac{4.2687 \times 10^6}{(T_l - 273.15)^2} + \frac{2.6754 \times 10^3}{T_l - 273.15} + 0.2575$

The total flux q_{wall} is divided between the gas and solid phases according to the weighting factor α_{wall}. h_{wall}, T_{wall} and α_{wall} are 20 W/m^2·K, 298 K and 0.5 respectively. In each row of computational cells, the total gas and solid flux components, $Q_{g,wall}$ and $Q_{s,wall}$, to be added as source terms to the enthalpy equations, are calculated by Eq. (11).

$$Q_{g,wall} = (1 - \alpha_{wall}) q_{wall} A_{wall} \quad \text{and}$$
$$Q_{s,wall} = \alpha_{wall} q_{wall} A_{wall} \quad \text{.....(11)}$$

These sources are distributed over the control volumes within 1 m of the wall. This wall flux distribution is necessary to give a source which varies smoothly from layer to layer in the orthogonal computational grid, where the inclined wall is represented by a stepped boundary.

Species boundary conditions are specified ore and coke compositions at the burden surface, and specified blast and PC compositions at the tuyere.

3. Base Results

The base calculation used geometrical and operational data from a blast furnace of inner volume 4 907 m^3 operating at a metal productivity of 2.19 t/m^3/day. Operational data and bulk solid properties at the burden surface are as described in Ref. 4).

The calculated gas phase mass fractions of CO and CO_2 are shown in **Fig. 1**. In this and subsequent figures, only half of a vertical cross-section of the furnace is shown and the deadman, raceway and cohesive zone (CZ) are indicated by dashed lines. CO concentration is greatest in the CZ, due to its generation by direct reduction, solution loss and the water gas reaction. It decreases as the gas ascends the furnace due to consumption by indirect reduction reactions. Conversely,

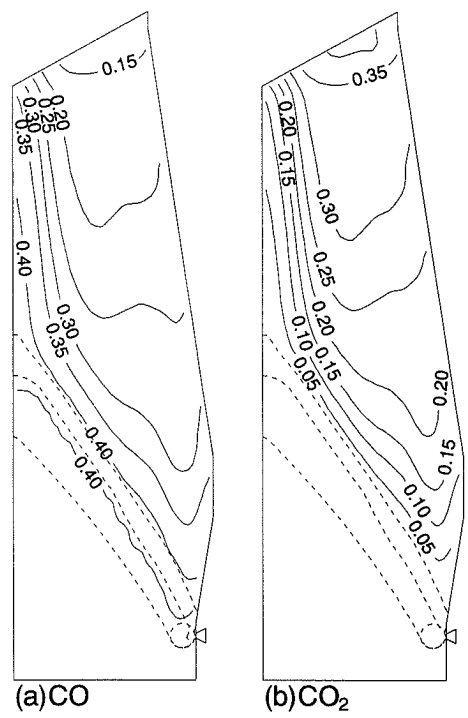

Fig. 1. CO and CO_2 gas phase mass fractions for the base case.

CO_2 concentration gradually increases as the gas ascends, being produced by the indirect reduction reactions. Near the furnace axis, CO_2 concentration is low as the ore volume fraction is low thus the volumetric rate of reduction is small.

The degrees of transformation for the three stages of iron reduction are shown in **Fig. 2**. Hematite is quickly reduced to magnetite after the solid enters the furnace. The endothermic magnetite–wustite and wustite–iron reduction reactions are much slower. Over the outer two-thirds of the furnace radius the onset of reduction is much slower due to the higher ore volume fraction in this region.

The phase mass fraction of carbon dissolved in liquid and fines volume fraction are shown in **Fig. 3**. Liquid carbon gradually increases, although below the raceway the liquid residence time is short and the carbon content does not reach the aim value. Regarding fines, the fines carbon is quickly combusted as the PC enters the raceway. Ash then melts due to the high fines temperature. In the present calculation, 90% of fines C and 73% of fines ash were consumed in and around the raceway, leaving only 11% of the injected fines mass exiting the raceway. The present raceway reaction rate equations result in a small local accumulation of fines above the point where the deadman joins the back of the raceway, but overall a fairly uniform distribution of fines exiting the raceway. This is in contrast to the result shown in Fig. 5d of Ref. 4), where the empirical source term resulted in most of the fines exiting the raceway almost directly opposite the tuyere, with a strong accumulation of fines at the point where the fines leave the raceway and enter the packed bed. This difference in fines outflow from the raceway then leads to different predicted fines dynamic holdup patterns in the shaft. The previous case showed a fairly narrow stream of concentrated fines ascending through the furnace, whereas the present calculation shows a more uniform pattern of fines dynamic holdup. While in the present calculation, this difference does not result in appreciable change in the predicted furnace state, at high PC rates the pattern of fines exit from the raceway may have a large influence on furnace stability due to possible PC char deposition throughout the shaft, particularly in and around the CZ. Thus, the present raceway PC reaction rate equations are probably too simplistic and should be improved to ensure more accurate results at high PC rates.

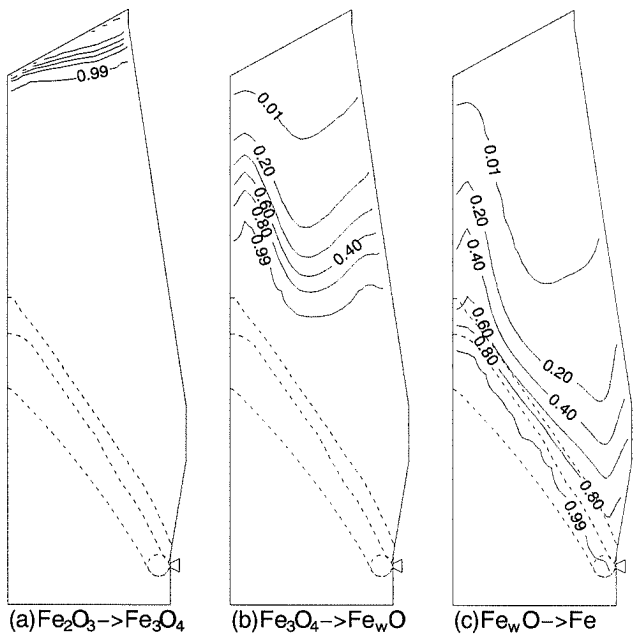

Fig. 2. Degree of transformation from (a) hematite to magnetite, (b) magnetite to wustite and (c) wustite to iron for the base case.

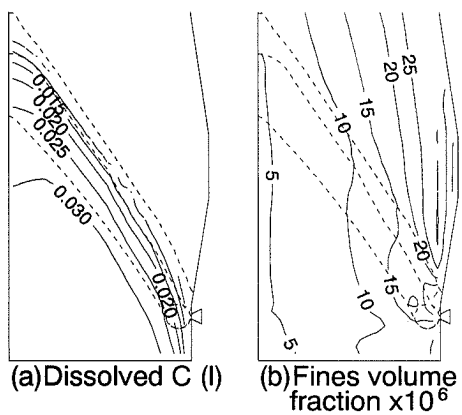

Fig. 3. (a) Phase mass fraction of carbon dissolved in liquid and (b) fines volume fraction for the base case.

4. Silicon Transfer

In the base case, the predicted temperatures below the CZ are higher than measured in actual furnaces. A possible reason for this is the neglect of silicon transfer processes. The reduction of silica is an endothermic reaction which occurs in the lower zone of the furnace. Silica is reduced to either solid SiC or gaseous SiO. SiO can be reduced with dissolved carbon in liquid metal, giving dissolved silicon. To test the effect of silicon transfer reactions on the model predictions, a silicon transfer submodel was added to the base model. The species added to the model are listed in **Table 4**. The reactions added to the model are listed in **Table 5**. The silicon species' boundary conditions are assumed ore and coke silica contents at the burden surface (50% by weight of gangue and ash respectively) and no SiO in the blast.

The calculated solids isotherms for the base case and the silicon transfer case are shown in **Fig. 4**. The temperature in the bosh is reduced by the endothermic silica reduction. The CZ is predicted to be slightly higher when silicon transfer is considered, due to the exothermic

Table 4. Chemical species added for the silicon model.

Species	Phase	S_{ψ}
SiO_2 (gangue)	solid	$M_{SiO_2}(-R_{21})$
SiO_2 (ash)	solid	$M_{SiO_2}(-R_{22}-R_{23}-R_{24})$
SiC	solid	$M_{SiC}(R_{24}-R_{25})$
SiO	gas	$M_{SiO}(R_{23}+R_{25}+R_{26}-R_{27})$
SiO_2 (slag)	liquid	$M_{SiO_2}(R_{21}+R_{22}-R_{26})$
Si	liquid	$M_{Si}(R_{27})$

Table 5. Chemical reactions and phase transformations added for the silicon model.

n	Formula	R_n (kmol/m^3·s)	Ref.	Interphase Heat Source (J/kmol)
21	SiO_2 (gangue) → SiO_2 (l)	As per reactions 15 to 19	-	T_{min}=1100°C T_{max}=1200°C
22	SiO_2 (ash) → SiO_2 (l)			T_{min}=1800°C T_{max}=2000°C
23	SiO_2 (ash) + C (s) ↔ SiO (g) + CO (g)	$k_{23}\rho_s\left(\omega_{SiO_2,s} - P_{CO}P_{SiO}/K_{23}\right)$	5,6	$\Delta H^{T_s}_{SiO,g}\cdot M_{SiO} + \Delta H^{T_s}_{CO,g}\cdot M_{CO}$
24	SiO_2 (ash) + 3C (s) ↔ SiC (s) + 2CO (g)	$k_{24}\rho_s\left(\omega_{SiO_2,s} - \omega_{SiC,s}P_{CO}^{\ 2}/K_{24}\right)$	5,6	$2\Delta H^{T_s}_{CO,g}\cdot M_{CO}$
25	SiC (s) + CO (g) ↔ SiO (g) + 2C (s)	$k_{25}A_{coke}\,\rho_s\omega_{SiC,s}/M_{SiC}$	8	$\Delta H^{T_s}_{SiO,g}\cdot M_{SiO} - \Delta H^{T_s}_{CO,g}\cdot M_{CO}$
26a	SiO_2 (l) + C (s) → SiO (ads. l) + CO (ads. l)‡		7	$\Delta H_{26a} = \Delta H^{T_l}_{SiO,g}\cdot M_{SiO} + \Delta H^{T_l}_{CO,g}\cdot M_{CO} - \Delta H^{T_l}_{SiO_2,l}\cdot M_{SiO_2}$
26b	SiO (ads. l) + CO (ads. l)‡ → SiO (g) + CO (g)	†$k_{26}A_{coke,slag}\,\alpha_{SiO_2,slag}/M_{SiO_2}$		$\Delta H_{26b} = \Delta H^{T_l}_{SiO,g}\cdot M_{SiO} + \Delta H^{T_l}_{CO,g}\cdot M_{CO}$
27	SiO (g) + C (l) → Si (l) +CO (g)	$k_{27}A_{coke,metal}\,\rho_g\omega_{SiO,g}/M_{SiO}$	9	$\Delta H^{T_s}_{CO,g}\cdot M_{CO} - \Delta H^{T_s}_{SiO,g}\cdot M_{SiO}$

†$\log_{10}\left(\alpha_{SiO_2,slag}\right) = 0.797 - 9.31\times10^{-4}\left(T_l - 273.15\right) - B\left[0.0228 + 8\times10^{-6}\left(T_l - 273.15\right)\right]$

where the slag parameter B is given by $B = \%CaO + \frac{\%Al_2O_3}{2} + \frac{\%MgO}{3} - \%SiO_2$.

‡ads. l : adsorbed on liquid

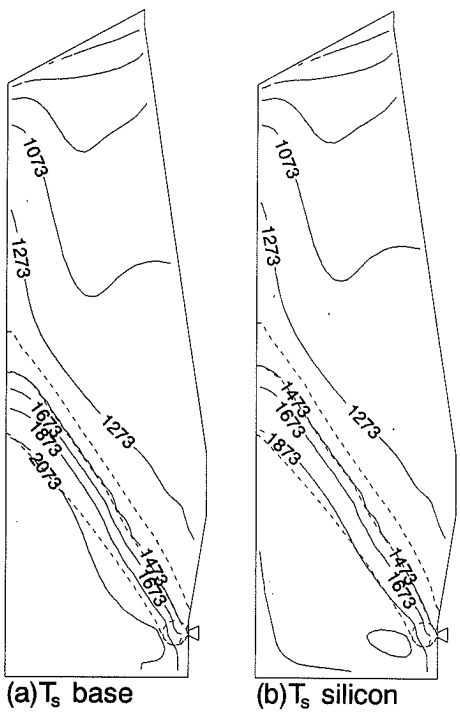

Fig. 4. Solid temperatures (K) for (a) the base case and (b) including silicon transfer.

re-oxidation of SiO which ascends from the bosh. The calculated average top gas and liquid outflow temperature are 530 K (257°C) and 1 942 K (1 669°C) compared to the base case values of 524 K (251°C) and 1 957 K (1 684°C) respectively. The liquid temperature has decreased slightly, with a corresponding increase in top gas temperature.

The phase mass fractions of coke ash silica, molten silica, gaseous SiO and dissolved Si are shown in **Fig. 5**. The reaction rates for SiO generation from coke ash silica and slag silica are shown in **Fig. 6**. The model predicts two regions of high SiO concentration. The first is above the raceway and along the deadman surface. This region shows where descending coke meets the ascending hot gases from the raceway, and coke ash SiO_2 is reduced to SiO. Ascending SiO then re-oxides to SiO_2 in and below the CZ as the gas temperature decreases. The second region of high SiO concentration is in the lower deadman near the axis, where molten silica reaches its maximum temperature. Some SiO is formed in this region, but SiO is also carried to this region from the raceway, particularly SiO formed from slag silica reduction behind and below the raceway. In the deadman, SiO has a relatively long residence time, hence the dissolved Si is a maximum here also. In contrast, the SiO generated from coke ash silica has a very brief contact time with molten metal, hence the low Si concentration near the raceway and along the deadman surface. The calculated average hot metal silicon content entering the hearth is 0.34%. This value is comparable to the measured value of 0.41% for this set of operational data.

5. Conclusions

A mathematical model of the blast furnace has been developed which calculates the steady state composition, motion, and temperature of gas, solid, liquid and fines phases. The model considers multiphase chemical reactions with rates calculated by chemical kinetic equations. The model predicts rapid initial reduction of hematite to magnetite, but slow reduction from magnetite to iron due to the endothermic nature of the reactions. Predicted gas and liquid phase compositions are plausible, but the fines dynamic holdup distribution is sensitive to the fines consumption processes in the raceway.

The model has also been extended to include silicon transfer. In the case studied in this report, the inclusion of silicon transfer results in a cooler bosh due to silica reduction, giving a slightly lower liquid outflow temperature than that calculated in the base case, and a higher CZ due to the exothermic SiO re-oxidation. Coke ash silica and molten slag silica both contribute to SiO generation, however in the present calculation hot metal silicon is more strongly dependent on slag silica due to longer SiO-metal contact times.

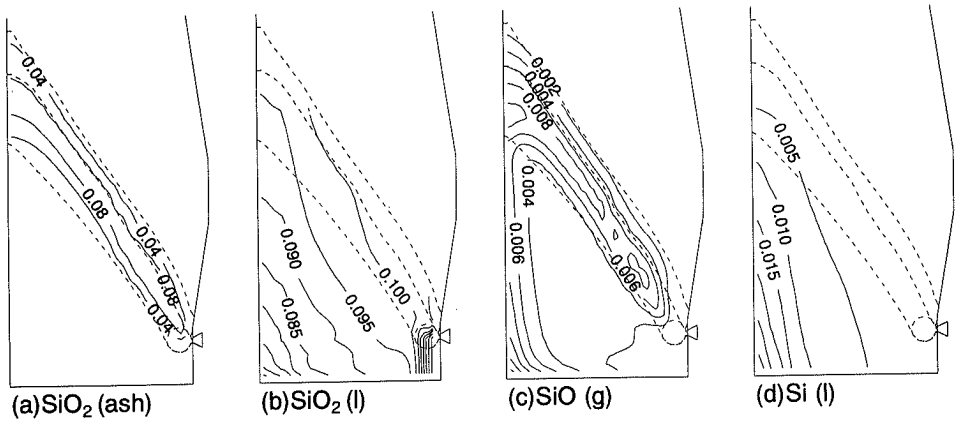

Fig. 5. Phase mass fractions of coke ash silica (s), slag silica (l), SiO (g) and Si (l).

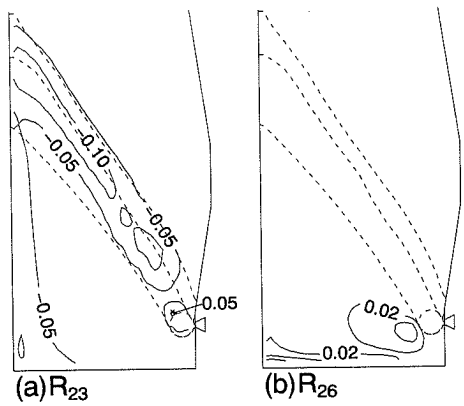

Fig. 6. Reactions rates (mol/m^3·s) for (a) coke ash silica to SiO and (b) slag silica to SiO.

Acknowledgement

The authors gratefully acknowledge NKK Corporation for supplying blast furnace geometrical and operational data.

Nomenclature

A_{face}: area of control volume face (m^2)
A_{ij}: contact area between phases i and j (m^2/m^3)
A_i: specific surface area of phase i (m^2/m^3)
$C_{P,i}$: heat capacity of phase i (J/kg·K)
D_n: diffusivity for reaction n in shrinking core reaction model (m^2/s)
d_i: mean particle diameter for phase i (m)
d_j: diameter of unreacted core of species j in shrinking core reaction model (m)
$\dot{E}_{ij}$: volumetric enthalpy flux from phase i to phase j (W/m^3)
$\tilde{F}_{ij}$: volumetric momentum flux from phase i to phase j (N/m^3)
Fr_{ij}: Froude number for phases i and j (—)
f_j: volume fraction of j in solid phase (—)
$\tilde{g}$: gravitational acceleration (m/s^2)
H_i: enthalpy for phase i (J/kg)
ΔH_n: interphase heat source for reaction n (J/kmol)
$\Delta H^T_{j,i}$: heat of formation for species j in phase i at temperature T (J/kg)
h_{ij}: heat transfer coefficient (W/m^2·K)
K_n: equilibrium constant for reaction n (—)
$k_{film,j}$: film mass transfer resistance for species j in shrinking core reaction model (m/s)
k_i: thermal conductivity of phase i (W/m·K)
k_n: kinetic constant for reaction n (various)
M_j: molecular weight of species j (kg/kmol)
P_i: pressure in phase i (Pa)
Pr_i: Prandtl number of phase i (—)
q_{wall}: wall heat flux (W/m^2)
R: gas constant (J/kmol·K)
R_n: rate of reaction n (kmol/m^3·s)
Re_{ij}: Reynolds number for phases i and j (—)
r: radial spatial coordinate (m)
S_ψ: source term for variable ψ
T_i: temperature of phase i (K)
$\tilde{u}_i$: interstitial velocity vector of phase i (m/s)
u_i: interstitial axial velocity component of phase i (m/s)
Vol_{cell}: volume of control volume (m^3)
v_i: interstitial radial velocity component of phase i (m/s)
We_{ij}: Weber number for phases i and j (—)
w: wustite stoichiometric constant (—)
x: axial spatial coordinate (m)

Greek Symbols

Γ_ψ: exchange coefficient for variable ψ
ε_i: volume fraction of phase i (m^3i/m^3 bed)
θ_{ij}: contact angle between phases i and j (°)
μ_i: viscosity of phase i (Pa·s)
ρ_i: density of phase i (kg/m^3)
ϕ_i: particle shape factor for phase i (—)
ψ: general dependent variable in Eq. (1)
$\omega_{j,i}$: mass fraction of species j in phase i (—)

Subscripts

f: fines
g: gas
l: liquid
s: solid

REFERENCES

1) M. Hatano and K. Kurita: *Tetsu-to-Hagané*, **66** (1980), 1898.
2) T. Sugiyama and M. Sugata: *Seitetsu Kenkyu*, (1987), No. 325, 34.
3) K. Takatani, T. Inada and Y. Ujisawa: *CAMP-ISIJ*, **7** (1994), 50.
4) P. R. Austin, H. Nogami and J. Yagi: *ISIJ Int.*, **37** (1997), 458.
5) E. T. Turkdogan, G. J. W. Kor and R. J. Fruehan: *Iron Steelmaker*, **7** (1980), 268.
6) C. Yamagata, Y. Kajiwara and S. Suyama: *Tetsu-to-Hagané*, **73** (1987), 637.

7) S. Taguchi, H. Kubo, N. Tsuchiya, K. Ichifuji and K. Okabe: *Tetsu-to-Hagané*, **68** (1982), 2303.
8) H. Inoue, T. Terui, J. Jeng, Y. Omori and M. Ohtani: *Res. Inst. Min. Dress. Met.*, **43** (1987), 43.
9) B. Ozturk and R. J. Fruehan: Process Tech Proc. 5th NISC AIME, **6** (1986), 959.
10) J. Chen, T. Akiyama, H. Nogami, J. Yagi and R. Takahashi: *ISIJ Int.*, **33** (1993), 664.
11) D. Kunii and J. M. Smith: *AIChE J.*, **6** (1952), 97.
12) S. Yagi, D. Kunii and Y. Shimomura: *Kagaku Kōgaku*, **21** (1957), 342.
13) W. E. Ranz and W. R. Marshall: *Chem. Eng. Prog.*, **48** (1952), 141; 173.
14) T. Akiyama, R. Takahashi and J. Yagi: *ISIJ Int.*, **33** (1993), 703.
15) E. R. G. Eckert and R. M. Drake: Heat and Mass Transfer, 2nd Ed., McGraw-Hill, New York, (1959), 173.
16) J. A. M. Kuipers, W. Prings and W. P. M. van Swaaji: *AIChE J.*, **38** (1992), 1079.
17) M. Niu, T. Akiyama, R. Takahashi and J. Yagi: *Tetsu-to-Hagané*, **82** (1996), 647.
18) P. J. Mackey and N. A. Warner: *Metall. Trans.*, **3** (1972), 1792.
19) Y. Hara, M. Tsuchiya and S. Kondo: *Tetsu-to-Hagané*, **60** (1974), 1261.
20) R. Takahashi, Y. Takahashi, J. Yagi and Y. Omori: *Ironmaking Conf. Proc.*, **43** (1984), 485.
21) Y. Omori: Blast Furnace Phenomena and Modelling, Elsevier, London, (1987), 129.
22) F. Fun: *Metall. Trans.*, **1** (1970), 2537.
23) S. Kobayashi and Y. Omori: *Tetsu-to-Hagané*, **63** (1977), 1081.
24) N. Miyasaka and S. Kondo: *Tetsu-to-Hagané*, **54** (1968), 1427.
25) C. R. Wilke: *J. Chem. Phys.*, **18** (1950), 517.
26) R. B. Bird, W. E. Stewart and E. N. Lightfoot: Transport Phenomena , Wiley Int., New York, (1960), 24; 258.
27) J. O. Hirschfelder, R. B. Bird and E. L. Spotz: *Chem. Revs.*, **44** (1949), 205.
28) Chemical Engineering Handbook, Chemical Engineering Society of Japan, Tokyo, (1988), 29.
29) R. H. Perry and D. Green: Perry's Chemical Engineers Handbook, 6th Ed., McGraw-Hill, New York, (1984).
30) T. Sugiyama, T. Nakagawa, H. Sibaike and Y. Oda: *Tetsu-to-Hagané*, **73** (1987), 2044.
31) K. Ishii, T. Itabashi, Y. Sazaki and Y. Kashiwaya: Four Fluid Flow and Heat Transfer Phenomena in Blast Furnace, ISIJ, Tokyo, (1996), 171.